

1 **Mapping land degradation risk due to land susceptibility to dust emission and**  
2 **water erosion**

3 Mahdi Boroughani<sup>1\*</sup>, Fahimeh Mirchooli<sup>1, 2</sup>, Mojtaba Hadavifar<sup>3</sup>, Stephanie Fiedler<sup>4</sup>

4 <sup>1</sup>Research Center for Geoscience and Social Studies, Hakim Sabzevari  
5 University, Sabzevar, Iran.

6 <sup>2</sup>Lab Expert, Sari agricultural Science and Natural Resources University, Sari,  
7 Iran

8 <sup>3</sup>Environmental Sciences Department, Hakim Sabzevari University, Sabzevar,  
9 Iran

10 <sup>4</sup>GEOMAR Helmholtz Centre for Ocean Research Kiel & Faculty of  
11 Mathematics and Natural Sciences, Christian-Albrechts-University of Kiel,  
12 Germany

13 (Corresponding Author: m.boroughani@hsu.ac.ir)

14  
15 **Abstract**

16 Land degradation is a cause of many social, economic, and environmental problems.  
17 Therefore identification and monitoring of high-risk areas for land degradation are  
18 necessary. Despite the importance of land degradation due to wind and water erosion  
19 in some areas of the world, the combined study of both ways of erosion on the same  
20 area receives relatively little attention. The present study aims to create a land  
21 degradation map in terms of soil erosion caused by wind and water erosion of semi-dry  
22 land. We focus on the Lut watershed in Iran encompassing the Lut Desert that is  
23 influenced by both monsoon rainfalls and dust storms. Dust sources are identified using  
24 MODIS satellite images with the help of four different indices to quantify uncertainty.  
25 The dust source maps are assessed with three machine learning algorithms  
26 encompassing artificial neural network (ANN), random forest (RF), and flexible  
27 discriminant analysis (FDA) to map dust sources paired with soil erosion susceptibility  
28 due to water. We assess the accuracy of the maps from the machine learning results  
29 with the metric Area Under the Curve (AUC) of the Receiver Operating Characteristic  
30 (ROC). The water and aeolian soil erosion maps are used to identify different classes  
31 of land degradation risks. The results show that 43% of the watershed is prone to land  
32 degradation in terms of both aeolian and water erosion. Most regions (45%) have a risk  
33 of water erosion and some regions (7%) a risk of aeolian erosion. Only a small fraction  
34 (4%) of the total area of the region had a low to very low susceptibility for land  
35 degradation. The results of this study underline the risk of land degradation for in an inhabited  
36 region in Iran. Future work should focus on land degradation associated with soil erosion  
37 from water and storms in larger regions to evaluate the risks also elsewhere.

38

39 Key words: Desertification, Desert-dust sources, Risk susceptibility, Water-induced  
40 soil erosion,

41

## 42 **Introduction**

43 Land degradation is one of the most pressing environmental issues around the globe.  
44 Several aspects of this issue have been recognized by the United Nations Convention  
45 (Gholami et al. 2019a). Land degradation can be driven by both water and wind, of  
46 which the former can have a stronger impact on soil erosion in a short time (Gia et al.  
47 2018). A total of 30% of global land area and three billion people are affected by land  
48 degradation (Wieland et al., 2019). In Iran, it is estimated that land and water  
49 degradation cost about US \$12.8 billion per year which is four percent of the total Gross  
50 Domestic Product (GDP) (Emadodin et al. 2012). Therefore, spatial mapping of risks  
51 of land degradation is necessary which can provide a basis to support managers and  
52 policymakers in risk mitigation and adaptation to aeolian and water erosion.

53 Land degradation driven by aeolian erosion is a known problem (Shi et al. 2004). Dust  
54 storms, which are a natural hazard, are associated with soil erosion. This phenomenon  
55 has detrimental impacts on the Earth system, e.g., for food security (Boroughani et al.  
56 2022), water supply (Duniway et al., 2019), human health (Moridnejad et al., 2015),  
57 geochemical conditions (Gholami et al., 2020b), and the Earth's carbon cycle  
58 (Gherboudj et al., 2017). Identifying dust sources as potential areas of dust emission is  
59 therefore necessary for developing a better understanding of land degradation. Spatial  
60 mapping of dust source susceptibility areas (DSSAs) is a crucial step for erosion  
61 mitigation and watershed management.

62 In addition to soil erosion by wind, water-driven soil erosion is a known mechanism for  
63 soil degradation. This kind of soil erosion is a known environmental threat and can  
64 influence both terrestrial and aquatic systems (Halecki et al. 2018, Sun et al. 2014).  
65 Therefore, knowing the spatial distribution of water-induced soil erosion susceptibility  
66 areas (SESA) is also necessary.

67 Different approaches for identifying DSSAs exist, e.g., using meteorological data  
68 (Yang et al. 2019), numerical modeling (Péré et al. 2018), and remote sensing (Jafari et  
69 al. 2021). Remote sensing can provide worldwide information on aerosol properties  
70 (Park et al. 2014). The present study uses Moderate Resolution Imaging  
71 Spectroradiometer MODIS satellite images in combination with machine learning to

72 detect dust aerosols and map its susceptibility over the Lut Desert. Moreover, several  
73 numerical models exist for predictions and risk evaluations of water-induced soil  
74 erosion (Chicas et al., 2016, Gao et al., 2017, Anache et al., 2018, Gia et al., 2018,  
75 Halecki et al., 2018), but none used machine learning to combine different  
76 observational data sets for assessing soil erosion. Machine learning has emerged as a  
77 subfield of data science and helps to better understand environmental problems  
78 (Gholami et al. 2019b). It can integrate data from different sources to create forecasts  
79 and discover patterns (Gholami et al. 2020a). In environmental sciences, algorithms  
80 such as support vector machine, random forest (RF), artificial neural networks (ANN),  
81 and multivariate adaptive regression spline have been applied, e.g., for groundwater  
82 (Lee et al. 2017), gully erosion (Zabihi et al. 2018), sediment contamination (Mirchooli  
83 et al. 2019), dust sources (Boroughani et al. 2020), landslides (Youssef and  
84 Pourghasemi 2021), floods (Tehrany et al. 2014), and trace elements (Derakhshan-  
85 Babaei et al. 2022).

86 However land susceptibility to soil erosion and dust emission has been assessed in  
87 different and separate studies, it has attracted less attention to investigate both of them  
88 in the same study. So, the novelty of this study lies in constructing an integrated  
89 framework based on field survey, different environmental factors, and machine learning  
90 algorithms to assess both of water erosion and dust emission.

91 This research is conducted to test some hypotheses including (1) the central and western  
92 parts of the watershed are the highest susceptible areas to water erosion and aerosol  
93 emission, respectively (2) NADI and land use are the most important factors for water  
94 erosion and aolian emission and (3) Central areas are the most prone parts of the  
95 watershed to these phenomena. Correspondingly, the aims of the current study are (1) to  
96 assess the spatially resolved contribution of soil erosion by water and wind using three  
97 machine learning algorithms, (2) determine the most important factor influencing water  
98 and dust emission susceptibility and (3) to combine the findings into spatially resolved  
99 information on risks for land degradation and recognize the hotspot area in terms of  
100 water erosion and dust emission.

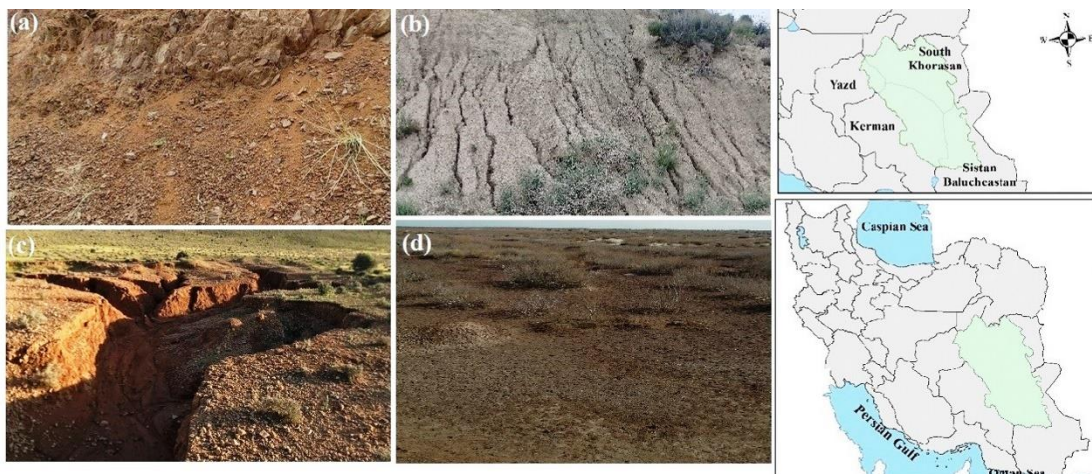
101

## 102 **2. Data and methods**

103 The focus of this study is on the Lut watershed situated in the east and southeast of Iran  
104 covering an area of 206242 km<sup>2</sup> ( 28° 10' to 32° 30' N latitude and 55° 45' to 61° 15' E  
105 longitude) and is marked in Fig. 1. This watershed include a great diversity of

106 topographic characteristics, with an elevation ranging from 124 to 4269m, and slope  
107 ranging from 0 to 28.04 degree. In this region, southwest and northeast aspects have  
108 the most frequencies (34% of the area). This watershed covers some parts of the South  
109 Khorasan, Yazd, Kerman, and Sistan-Baluchestan Provinces of Iran. In addition,  
110 several important cities and towns such as Birjand, Tabas, Bam located in the  
111 watershed. Aridisols is the dominant soil order of the watershed in which it constitutes  
112 40.1% of this region. The study watershed includes the largest desert of the country,  
113 the Lut Desert. The region contributes to the increasing dust concentration in southwest  
114 Asia (Ebrahimi-khusfi et al. 2021). This area is chosen to develop and test the methods  
115 based on regional data on erosion observations with examples shown in Fig. 1a-d. It  
116 underlines the impacts of land degradation that goes well beyond impacts on the natural  
117 environment.

118



119

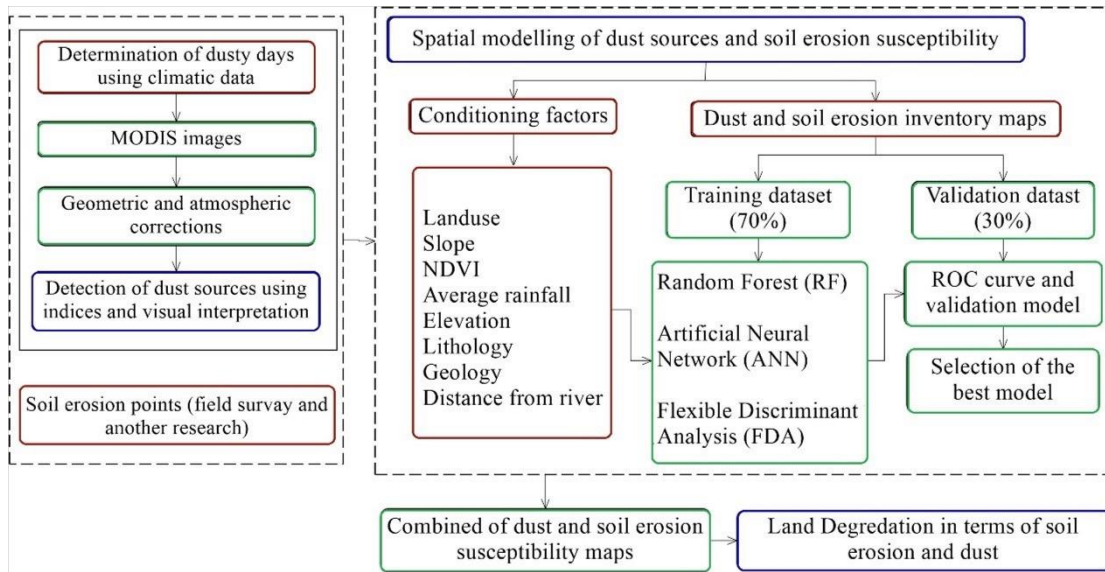
120 Fig.1 Geographical location of the study watershed. Green shading marks the Lut watershed. The Lut  
121 Desert is located in the centre of the watershed. Settlements are primarily situated in the northern and  
122 south-western parts. Example of soil erosion in the watershed are sheet erosion (a), rill erosion (b),  
123 gully erosion (c), and wind erosion (d).

124

## 125 2. 1. Land degradation mapping

126 Our land degradation zonation consists of three main processing steps, graphically  
127 depicted in Fig. 2. At first, spatial mapping of water erosion is conducted (section  
128 2.1.1). In the second step, spatial mapping of dust source susceptibility is carried out  
129 with machine learning methods (section 2.1.2). In the last step, the patterns of water  
130 erosion and dust source susceptibility are combined to identify risk areas of land  
131 degradation (section 2.2.3).

132



133

134

Fig.2 Flowchart of inputs (red boxes), data processing (green boxes), and outputs

135

(blue boxes) in the present study

136

137

### 138 2.1.1 water erosion map

139

140 Quantifying the erosion susceptibility of an area requires to determine a spatial  
141 distribution of observed water-induced soil erosion that can have different  
142 characteristics, e.g., gully erosion, rill erosion, and surface erosion. That information is  
143 extracted from data collected during an own field survey paired with previous research  
144 (Shit et al. 2020). In the previous research, a combination of consulting with provincial  
145 experts, satellite images, recent aerial photos, and field survey were applied to identify  
146 soil erosion. The aim of the field survey for the present study was to identify regions  
147 where sheet, rill, and gully erosion took place. This field survey was carried out in  
148 accessible parts of the watershed in April 2020. These accessible parts are mostly  
149 distributed around the cities (such as Bam, Ravar, Shahdad, Baravar, Birjand, Tabas,  
150 etc) with proper road access located in the watershed. The data set contains the type of  
151 water-induced soil erosion along with the geographical location using a Global  
152 Positioning System (GPS). A selection of the identified water soil erosions in the study  
153 region is shown in Fig. 1.

153

154 We translated the observations of the field survey into maps of non-degraded and  
155 degraded areas. These areas were plotted in an inventory map and prepared for further  
analysis, although not all desert areas are fully covered by the survey.

156

### 157 **2.1.2 Dust aerosol map**

158 The large desert area to be covered is a motivation for the use of satellite data for  
159 estimating dust sources. We used MODIS images from the Terra (morning) and Aqua  
160 (afternoon) satellites (Vickery and Eckardt, 2013) to identify dust aerosols. We define  
161 dusty days, when the horizontal visibility is less than 2000 m for at least one hour during  
162 the day based on available weather stations in Iran (Vickery and Eckardt, 2013;  
163 Boroughani et al., 2021). According to the mentioned condition, more than 500 dusty  
164 days were identified during 2010–2021 distributed over the stations in Birjand,  
165 Zahedan, Kerman, Bam, Doostabad, Bisheh, Rafsanjan and Mighan. We pair the station  
166 observations with satellite data to estimate the spatial extent of the dust aerosol plumes.  
167 Due to the overpass of the Terra and Aqua satellites once per day, we acquired 28  
168 satellite images from the MODIS sensor that during times when the weather stations  
169 had documented dusty conditions in the ten-year period. For identifying pixels with  
170 dust aerosols in these images, we calculate four different dust indices (BTD2931,  
171 BTD3132, NDDI and D) for dust aerosol identification (Borroughani et al., 2020, 2021  
172 Hahnenberger and Nicoll, 2014).

$$173 \quad B(T, \lambda) = \frac{2hc^2}{\lambda^5 \frac{hc}{(e\lambda kt - 1)}} \quad (1)$$

174 where  $B(T, \lambda)$  represents the Planck equation at  $\lambda$  ( $\mu\text{m}$ ),  $T$  is the BT (K),  $h$  is the  
175 Planck's constant ( $6.626 \times 10^{-34} \text{ m}^2\text{kgs}^{-1}$ ),  $k$  is the Boltzmann's constant ( $1.38 \times 10^{-23}$ )<sup>5</sup>,  $c$   
176 is the speed of light ( $2.99 \times 10^8 \text{ ms}^{-1}$ ), and  $T$  is the temperature (Hao et al., 2007)  
177

$$178 \quad T = \frac{hc}{\lambda k \ln(1 + \frac{2hc^2}{L\lambda^5})} \quad (2)$$

179 Using Planck's equation, the value of the temperature can be derived, where  $L$  is the  
180 amount of radiance in the images (in  $\text{Wm}^{-2}\text{sr}^{-1}\mu\text{m}^{-1}$ ).

181

$$182 \quad NDDI = (p_{2.13} - p_{0.469}) / (p_{2.13} + p_{0.469})$$

183 (3)

184

185 where  $p_{2.13}$  and  $p_{0.469}$  depict the reflectance value at the top-of-atmosphere at 2.13  
186 and 0.469  $\mu\text{m}$ , respectively (Qu et al., 2006)

187

$$188 \quad D = \exp\{-[rr \times a + (BTD - b)]\} \quad (4)$$

189 where  $rr$  shows the reflectance proportion among wavelengths of 0.54  $\mu\text{m}$  and 0.86  $\mu\text{m}$   
190 and  $BTD$  is the difference among the bands 11 and 12  $\mu\text{m}$ ;  $a$  and  $b$  are constants taken

191 during the initial calibration (Eq. 1). (Qu et al., 2006; Miller, 2003; Hao et al., 2007;  
192 Boroughani et al., 2020, 2021).

193 We compute false color maps using four combinations of channels (1: NDDI, B4, B3;  
194 2: D, BTM2931, NDDI; 3: D, BTM3132, NDDI; and 4: BTM2931, B4, B3) in ENVI  
195 software. We choose these four different indices for cross-validating the presence of  
196 dust aerosols. With each of these methods we see dust aerosol in different color and  
197 qualities in the MODIS images over 28 days. After combining the four methods in the  
198 software ENVI, we choose the method that shows the dust plume in the MODIS image  
199 more clearly as the best method (Boroughani et al., 2020, 2022). This method is based  
200 on a cone of dust diffusion seen in the processed MODIS images, where the apex  
201 denotes the dust's source (Lee et al., 2009; Walker et al., 2009). Ultimately, the  
202 inventory map of the dust aerosols in the Lut watershed was created.

203

## 204 **2.2. Identification of key factors controlling for aeolian and water erosion**

205 To develop DSSA and SESA, the identification and selection of appropriate dust  
206 sources and soil erosion effective factors are necessary. The main factors affecting  
207 DSSA and SESA were selected and constructed based on literature, available data and  
208 geographical maps (Torabi et al., 2021; Zabihi et al., 2018; Boroughani et al., 2020;  
209 Gholami et al., 2020a). The considered factors in this study included: elevation, land  
210 use, slope of terrain, lithology, annual rainfall, distance from rivers, and distance from  
211 roads, the Topographic Wetness Index (TWI), and Normalized Difference Vegetation  
212 Index (NDVI). Various sources were used to gather data for these factors, introduced  
213 in the following in more detail. All collected data were mapped to a horizontal grid of  
214 1km resolution.

215 The shuttle radar topography mission (SRTM) images were used to create the digital  
216 elevation model (DEM, Fig 3c) (Ghorbanzadeh et al., 2018). The lowest and highest  
217 elevation of the study area is 124 m in the centre of the desert and 3966 m at the western  
218 and eastern margins of the study watershed, respectively (Fig. 3c). Vegetation cover  
219 considerably supports soil conservation. Areas with low vegetation cover would be  
220 more sensitive to both erosion by water and wind (Arabameri et al., 2019a; Gholami et  
221 al. 2019b). Therefore, we use the Normalized Difference Vegetation Index (NDVI) to  
222 assess the vegetation cover in the study area from MODIS images following  
223 (Arabameri et al., 2019a; Boroughani et al., 2020):

224  $NDVI = \frac{NIR+R}{NIR-R}$

225 Where R is the red (0.620-0.670  $\mu\text{m}$ ) and NIR is near-infrared bands (0.841-0.876  $\mu\text{m}$ )  
226 (Fig. 3d).

227 Annual rainfall (Fig. 3e) was obtained from Iran Meteorological Organization for the  
228 period of 2000-2021. Mean annual rainfall was calculated using 40 different  
229 meteorological stations located within or close to the watershed (Fig.3e). The inverse  
230 distance weighting (IDW) interpolation method was applied to integrate rainfall over  
231 the study area in the ArcGIS environment (Gholami et al., 2020a). Topographic  
232 Wetness Index (TWI), which indicates the spatial distribution of areas of potential soil  
233 saturation, is an effective factor to indicate water erosion including landslides and also  
234 flooding (Arabameri et al., 2019b). TWI which determines the dry and wet zones  
235 calculated as (Beven and Kirkby 1979):

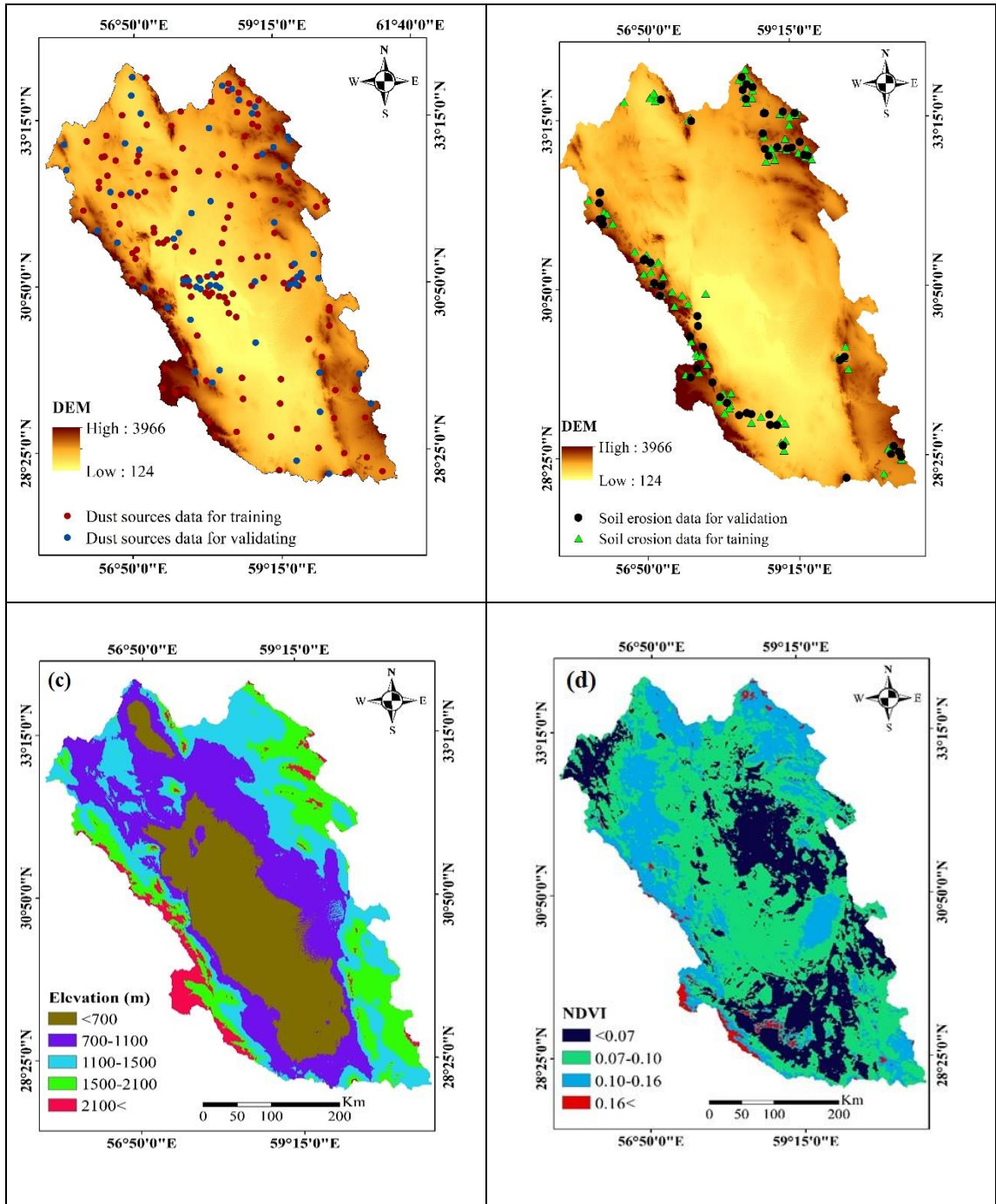
236  $TWI = \ln \left( \frac{\alpha}{\tan\beta} \right)$

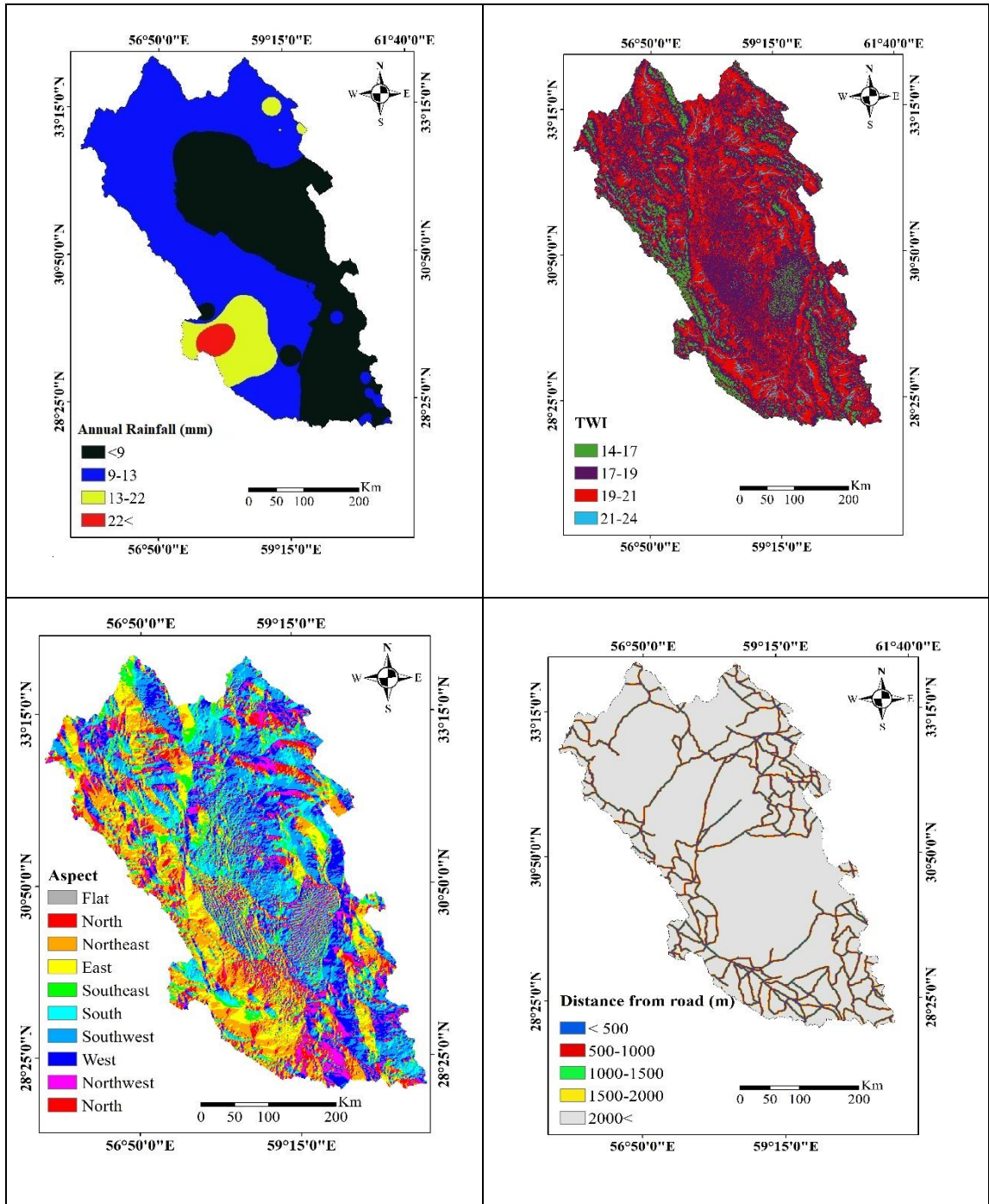
237 where  $\alpha$  is the cumulative up-slope area from a point (per unit contour length) and  $\beta$  is  
238 the slope angle at that point. This index was calculated in the SAGA-GIS environment  
239 and classified into four groups viz. 14-17, 17-19, 17-21, 21-24 (Fig. 3f). The aspect  
240 map was also generated using DEM and grouped into ten classes (Fig. 3 g). Distance  
241 from road is an indicator of infrastructure development which influences soil erosion  
242 and land degradation (Torabi et al., 2021). This factor is shown in five classes in Fig. 3  
243 h. Distance from river is one of the most effective factors on water-caused erosion  
244 (Amiri et al., 2019) which is classified into six groups (Fig. 3i).

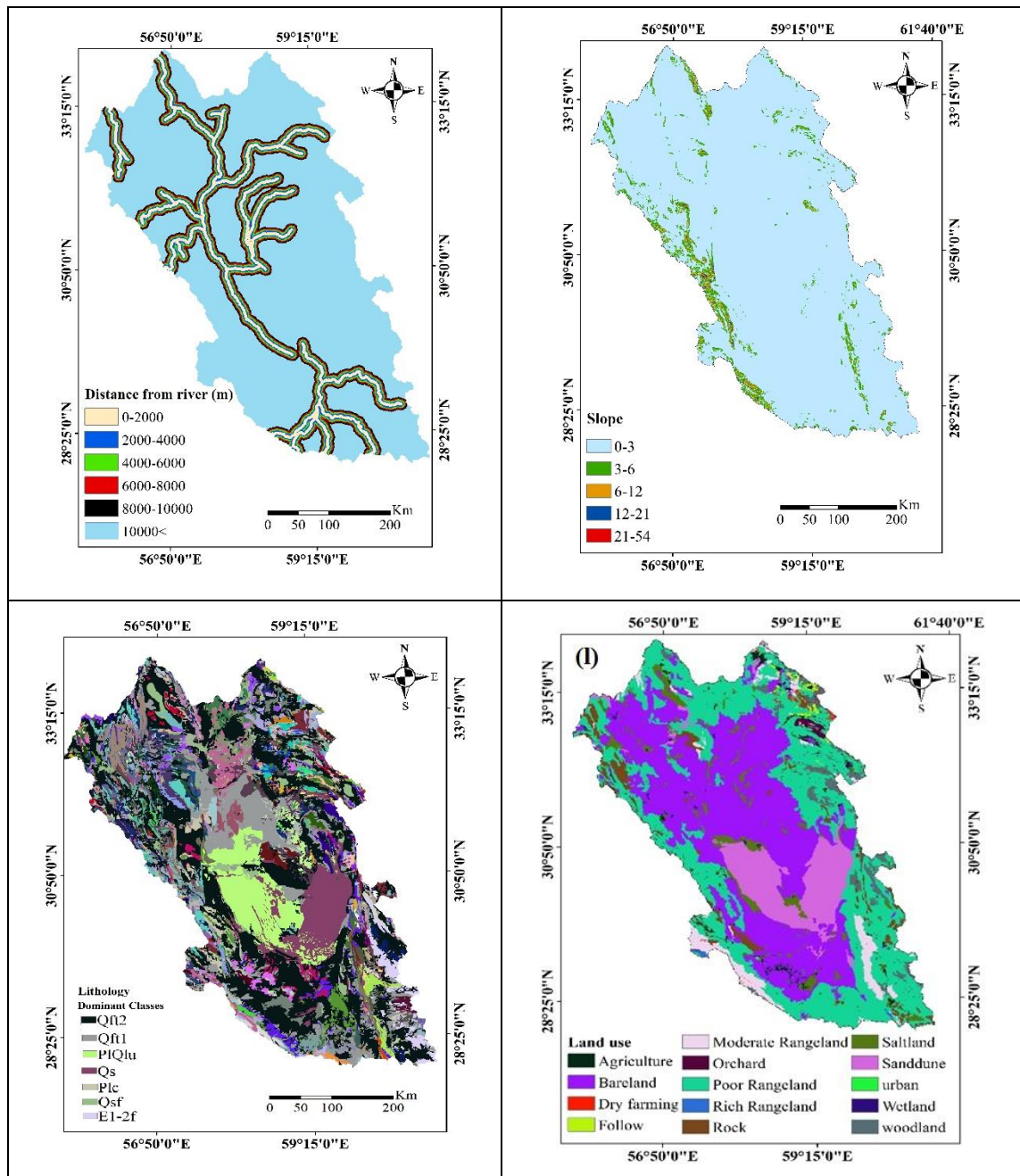
245 The slope map (%) was created using a Digital Elevation Map (DEM, Fig. j) and  
246 classified into five groups including 0-3%, 3-6%, 6-12%, 12-21%, and 21-54%. The  
247 lithology map indicates eleven different soil classes in the study area (Fig. 3k).

248 Land use and soil maps were obtained from base maps developed by the Iranian Forest,  
249 Rangeland, and Watershed Management Organization (<https://frw.ir/>). In the study  
250 region, there are fourteen land-use classes including wetlands, rangelands of three states  
251 (poor, medium, and rich), dry farming, agricultural lands, urban area, fallow land, rock-  
252 covered land, wetland, saltland, woodland, bare surfaces, and sand dunes (Fig. 3m). A  
253 large percentage (83%) of the watershed area is covered by bare land, poor rangeland,  
254 and sand dunes. All three land use classes are prone to wind erosion due to sparse or no  
255 vegetation.









256  
 257 Fig.3 Location of dust observation points for training and validation (a), water-induced soil erosion  
 258 points for training and validation (b), and the conditional factors (Elevation (c), NDVI (d), Rainfall (e),  
 259 TWI (f), Aspect (g), Distance from road (h), Distance from river (i), Slope (j), Lithology (k), Land use  
 260 (l)) in the watershed.

261

## 262 2.4. Spatial mapping of DSSA and SESA using machine learning algorithms

263 We combine the two susceptibility maps for DSSA and SESA to create the land  
 264 degradation hazard map with regards to water- and wind-induced soil erosion. For both  
 265 types of soil erosion, three machine learning models were constructed and applied. The  
 266 land degradation susceptibility map was then created by synthesizing the results for

267 both soil erosion types in an ArcGIS 10.5 environment, and the land degradation  
268 susceptibility was ultimately evaluated with four classes.

269 A wide range of machine learning algorithms has been applied for spatial mapping of  
270 environmental phenomena in the past. The effective factors described in Section 2.2  
271 and the inventory maps of water and wind erosion were used as the input of the machine  
272 learning algorithms. In the present study, the algorithms of random forest (RF), artificial  
273 neural network (ANN), and flexible discriminate analyses (FDA) were used to produce  
274 DSSA and SESA maps. We choose three different algorithms to test the dependency of  
275 the results on the method as a measure of uncertainty. The three algorithms are  
276 described in more detail in the following.

277

#### 278 **2.4.1 Random forest (RF)**

279 Random forest developed by Breiman (2001) is a machine learning algorithm for non-  
280 parametric multivariate classification. RF builds multiple trees using a random  
281 selection of the training dataset. The data not included are called out-of- bag (OOB)  
282 determines the model accuracy using generalization error estimation (Breiman 2001).  
283 Diversity among the classification trees increases using resampling the data with  
284 replacement and also randomly change of predictors set during tree induction processes  
285 (Youssef et al., 2016). Information from numerous decision trees has been combined in  
286 the RF algorithm.

287 Generally, it is essential to define two parameters to run the RF model including the  
288 number of trees (ntree) and the number of factors prepared from the data shown in Fig.  
289 3 (mtry). The former is built while the RF model is running, while the latter is used in  
290 the tree-building process. Both the number of trees and factors need to be optimized to  
291 minimize the generalization error (Rahmati et al. 2016). The optimisation was done  
292 through sensitivity tests.

293

#### 294 **2.4.2 Artificial neural network (ANN)**

295 The artificial neural network (ANN) is a machine learning tool developed by imitating  
296 human brain performances and making connections between inputs and outputs  
297 (Sakizadeh et al. 2017). The human brain is mimicked in two ways: Firstly, obtaining  
298 information and knowledge using a learning process, and secondly, storing knowledge  
299 using synaptic weights. Therefore, ANN has been identified as the model that finds the  
300 optimal solution for non-linear problems, such as dust source and soil erosion

301 susceptibility, by identifying patterns with conditioning factors (Ghorbanzadeh et al.  
302 2019). In an ANN, a neuron is the smallest data processing unit which could make many  
303 neural network structures and be used in research for different purposes. The standard  
304 structure of ANN consists of three layers, namely, the input layer, the hidden layers,  
305 and the output layer. The input layer consists of training data and conditioning factors  
306 of dust source, the neurons in the hidden layer analyze the complex information  
307 contained in the data, and the output layer is the maps of dust source susceptibility. In  
308 this structure, the neurons across the same layer are not connected, but they are linked  
309 with neurons in the previous and subsequent layers. In ANN, the algorithm determines  
310 a weight for each input factor and a transfer function to build results (Kalantar et al.  
311 2017).

312

### 313 **2.4.3 Flexible discriminate analyses (FDA)**

314 The modification of the linear regression model for the application to non-linear  
315 problems is the purpose of FDA (Avand et al. 2021). Nonparametric regression models,  
316 nonlinear discriminant analysis, and classification methods are combined into one  
317 framework. This algorithm is flexible for non-linear classifications because non-linear  
318 transformation is used and clusters are soft (Kalantar et al. 2020), here clusters for the  
319 relationship between soil erosion and the predictor factors from Fig. 3. In this way,  
320 variables in FDA are firstly aligned with the multivariate adaptive regression splines  
321 (MARS) and then dimension reduction is performed (Kim and Kim 2021). FDA can  
322 overcome the problem of linear discriminant analysis (LDA) and it is minimizing the  
323 square average of the residuals (Mosavi et al. 2020), while linear regression is replaced  
324 by nonparametric regression in FDA. Therefore, FDA has the potential to apply for  
325 non-linear natural problems such as soil erosion, dust, flood, and landslide.

326

### 327 **2.5. Evaluation of machine learning algorithms**

328 In our DSSA and SESA assessment, 70% of point data are randomly selected for the  
329 training dataset and 30% for model validation. The prediction accuracy of the machine  
330 learning algorithms is assessed by comparing the DSSA map with the validation dataset  
331 of dust sources. These data were extracted from MODIS images and some indicators  
332 which were explained in section 2.1.2. The Receiver Operating Characteristic (ROC)  
333 curve and the Area Under the Curve (AUC) are applied following past studies that used  
334 these to test the prediction skill of a model for the occurrence or non-occurrence of the

335 studied phenomena (Naghibi et al. 2017). The AUC ranges from 0 to 1 in which the  
336 models that better perform represent the AUC close to one.

337

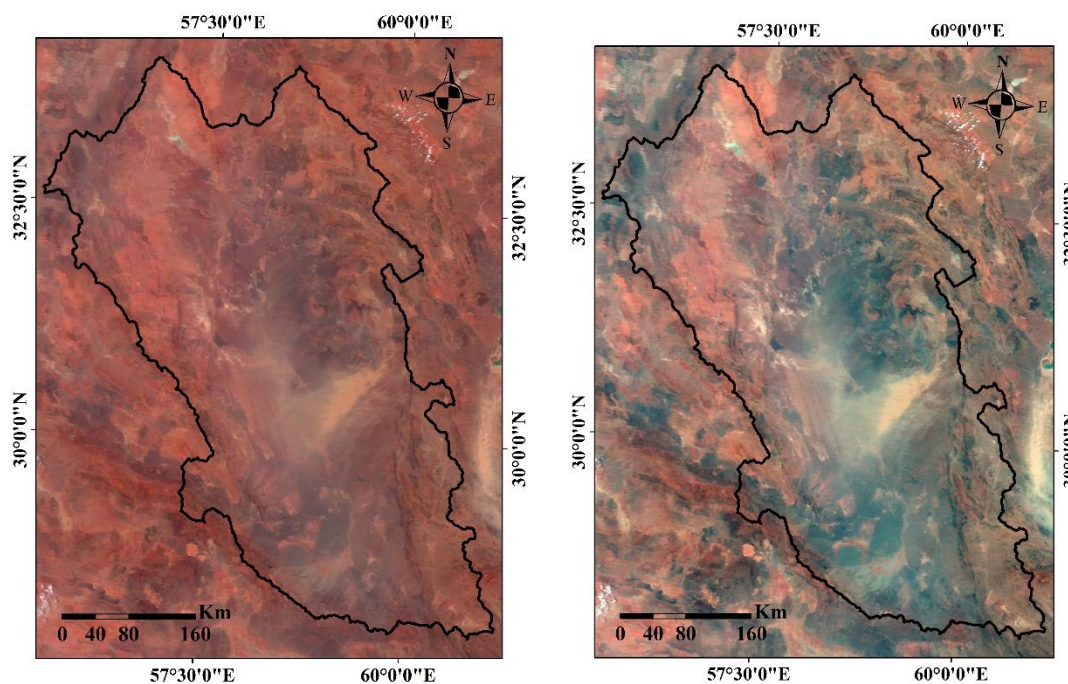
### 338 **3. Results and Discussion**

#### 339 **3.1. Spatial distribution of DSSA**

##### 340 **3.1.1. Dust aerosol detection**

341 An illustration of a dust storm seen in MODIS FCC satellite imagery over the Lut  
342 watershed on August 7, 2019, is shown in Fig. 4. Following a visual analysis of the  
343 images, we determined that the false colour combination (R: BTD2931, G: Band 4, B:  
344 Band 3) is the best and applied it to 26 MODIS images of dusty days. As a result, the  
345 Lut watershed's dust source locations were identified (Fig. 4).

346



347 Fig.4 The dust storm on 07 August 2019, as seen above is an example of the visual  
348 inspection of a dust storm (a) MODIS true colour (Red: Band 5, Green: Band 4, Blue:  
349 Band 3), and (b) enhanced MODIS satellite photos, (Red: BTD2931, Green: Band 4,  
350 Blue: Band 3).

351

##### 352 **3.1.2 The importance of conditioning factors for DSSA**

353 Since multicollinearity among factors has been identified as an obstacle to explaining  
354 the results (Roy and Saha 2019), the Variance Inflation Factor (VIF) was calculated to  
355 assess the relationships among conditioning factors. This was conducted because  
356 multicollinearity among factors will decline the accuracy of the models (Arabameri et  
357 al. 2019b). In the present study, VIF values for DSSA mapping range from 1.05 to 1.57  
358 which illustrated no collinearity among the eight factors. Therefore, no exclusion was  
359 applied and all factors were considered in successor calculations and modeling.

360 The importance and impact of each factor depend on the machine learning algorithms.  
361 The result of DSSA mapping using RF showed that NDVI, elevation, land use, and  
362 lithology had the greatest degree of effect among conditioning factors. Land use and  
363 NDVI as an index of vegetation cover proved to have a controlling impact on wind  
364 erosion and dust emission (Gholami et al., 2020). Elevation is an effective factor for  
365 DSSA in which lowlands have higher impacts than highlands. This was confirmed by  
366 other studies such as Darvand et al., 2021. Lithology is another important factor in this  
367 watershed since dust emission is mostly occur in the sensitive lithology rather than  
368 resistant ones (Sissakian et al., 2013). Overall, the impacts of these factors on DSSA  
369 have been proved by previous investigations (Gholami et al. 2020a, 2020b). Other  
370 factors such as the distance from rivers, rainfall, and slope were identified as rather  
371 weak predictors, respectively. These findings agree with other research (Boroughani  
372 and Pourhashemi 2020, Darvand et al. 2021).

373 The FDA approach showed that however elevation, NDVI, and land use had the highest  
374 effects on dust sources susceptibility, other factors had no impact on DSSA. Similarly,  
375 with ANN, elevation, NDVI, and land use were identified as the three most effective  
376 factors, and other factors were weaker predictors rather than formers. However these  
377 two models of FDA and ANN provide similar results in term of the importance of  
378 conditioning factors, FDA could be used rather than ANN because of its higher  
379 accuracy which is shown in the next section.

380

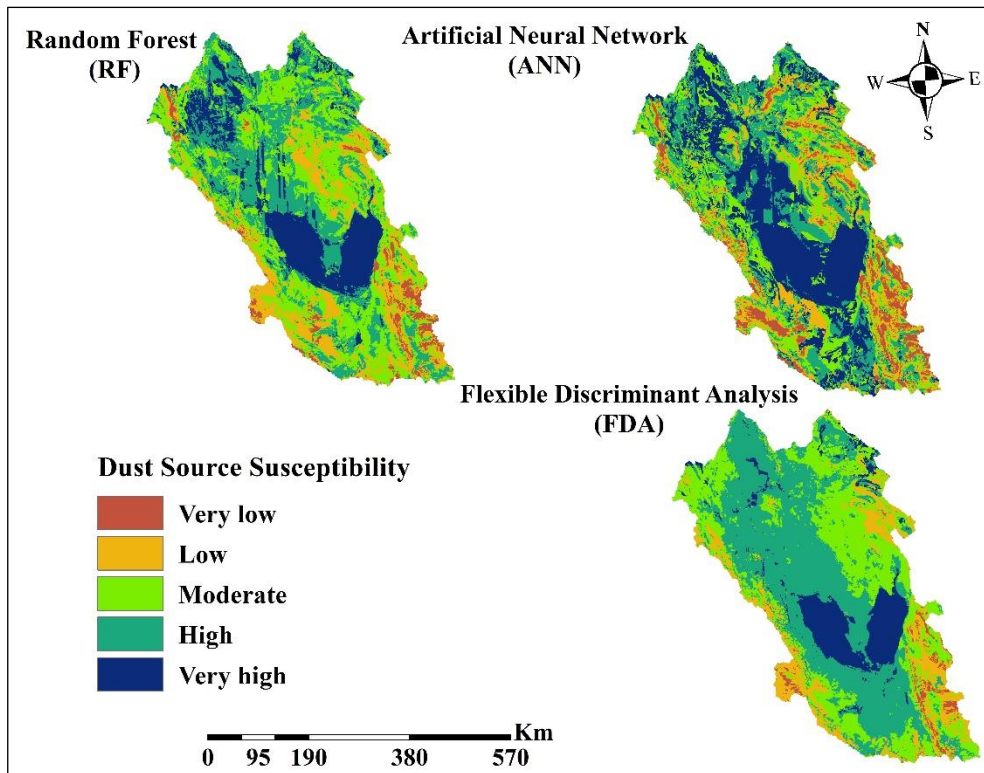
### 381 **3. 1. 3 Spatial distribution of dust source susceptibility**

382 The dust source susceptibility (DSS) maps created by RF, FDA, and ANN are classified  
383 into five risk classes (very high, high, moderate, low, and very low) shown in Fig. 5.  
384 These classes are set as in earlier studies (Mosavi et al., 2020; Boroughani,  
385 Mohammadi, Mirchooli, & Fiedler, 2022). The results of the model evaluation using  
386 ROC indicates that the RF model with an accuracy of 75.0% provides the most accurate

387 outputs. FDA and ANN had similar performances with the accuracy of 71.7% and  
388 70.7%. In terms of True Skill Statistic (TSS), similar results have been obtained in  
389 which RF with an accuracy of 45.8% had again the best performance in comparison to  
390 FDA (32.4%) and ANN (35.8%). In this way, RF introduces different priorities for the  
391 effective factors in comparison with FDA and ANN. RF proposes NDVI, elevation,  
392 land use, and lithology as the most important factors, while FDA and ANN suggest  
393 elevation, NDVI, and land use as the most influencing factors. The dominance of  
394 NDVI, elevation and land use as the most effective factors for DSS is consistent with  
395 the understanding of dust source locations that are typically found in topographic  
396 depressions with sparse or no vegetation. The DSSA map from RF was selected for  
397 further analysis due to the highest accuracy, although the differences between FDA and  
398 ANN are in the statistical sense relatively small. According to the DSSA maps, 29%  
399 and 17% of the watershed were classified as areas of high and very high DSSA, i.e.,  
400 almost half of the study area. Only 4% and 16% of the watershed have a very low and  
401 low susceptibility to soil erosion through winds, respectively. The spatial extent of high  
402 and very high risk areas from RF is smaller than the ones obtained by ANN and FDA.  
403 In all three maps, it can be seen that the biggest potential for dust emission is located in  
404 the central parts (Lut Desert) of the watershed. These results are consistent with other  
405 research, indicating that RF allows more detailed spatial mapping of dust source  
406 susceptibility compared to other machine learning algorithms (Rahmati et al. 2020,  
407 Gholami et al. 2019b, Darvand et al. 2021).

408





409

410

411

412

Fig. 5 Dust sources susceptibility area (DSSA) based on random forest (RF), artificial neural network (ANN), and flexible discriminate analyses (FDA)

413

As mentioned before, the watershed is one of the key regions with dust concentration in southwest Asia. Spatial distribution of dust sources in this region is a key roadmap for preventive and adaptive measurement. This would reduce dust emission across the watershed, region, and even other near countries.

417

### 418 3.2. Soil erosion susceptibility map

#### 419 3.2.1 Relative influential conditioning factors for SESA

420

There are some differences in the contributions of influential factors among models. So that, RF indicates that rainfall, TWI, slope, elevation, land use, and geology are the most important conditioning factors. Considering this watershed located in arid region of Iran, rainfall and TWI play decisive and crucial role in soil erosion among them. TWI which indicate soil moisture and water-saturated area (Silva et al., 2023) has been also identified an effective factor for different kinds of soil erosion such as rill-interrill, gully, and piping erosions (Sholagberu et al., 2017; Hosseinalizadeh et al., 2019). Slope influences also soil erosion rate through effecting on runoff velocity, vegetation cover, and soil type (Avand et al., 2022). This conditioning factor has been also reported as

428

429 one of the most influential factor in most studies (Sholagberu et al., 2017; Pournader et  
430 al., 2018; Lei et al., 2020). Moreover, distance from roads and rivers were recognized  
431 as the least important factors. These findings of the impact of conditioning factors for  
432 SESA are similar in other regions (Arabameri et al. 2019a, Hosseinalizadeh et al. 2019).  
433 For ANN, TWI, slope, and land use were the most effective factors for prediction which  
434 is followed by NDVI, land use, and distance from the river. The results from FDA  
435 indicated that the most important conditioning factors are TWI, slope, and elevation,  
436 geology, and NDVI. TWI has an important impact on SESA in all three models. This  
437 is because the study watershed predominates with low slopes and elevations. The  
438 opposite result of this finding was obtained by Silva et al., 2023.

439 A large area of the watershed is land with typically little rain and vegetation cover such  
440 that bare soil is the main physical attribute in the watershed. This kind of surface is  
441 known to be prone to water-induced soil erosion, when rain events occur. The erosion  
442 can be particularly pronounced over slopes. This understanding is consistent with all  
443 algorithms pointing to a major role of TWI and slope for SESA.

444 Some environmental factors (rainfall, TWI, slope, elevation, and geology) influence  
445 SESA more than DSSA. Land use as a human-induced conditioning factor, however,  
446 affects both SESA and DSSA, which underlines the importance of land-use planning  
447 and management.

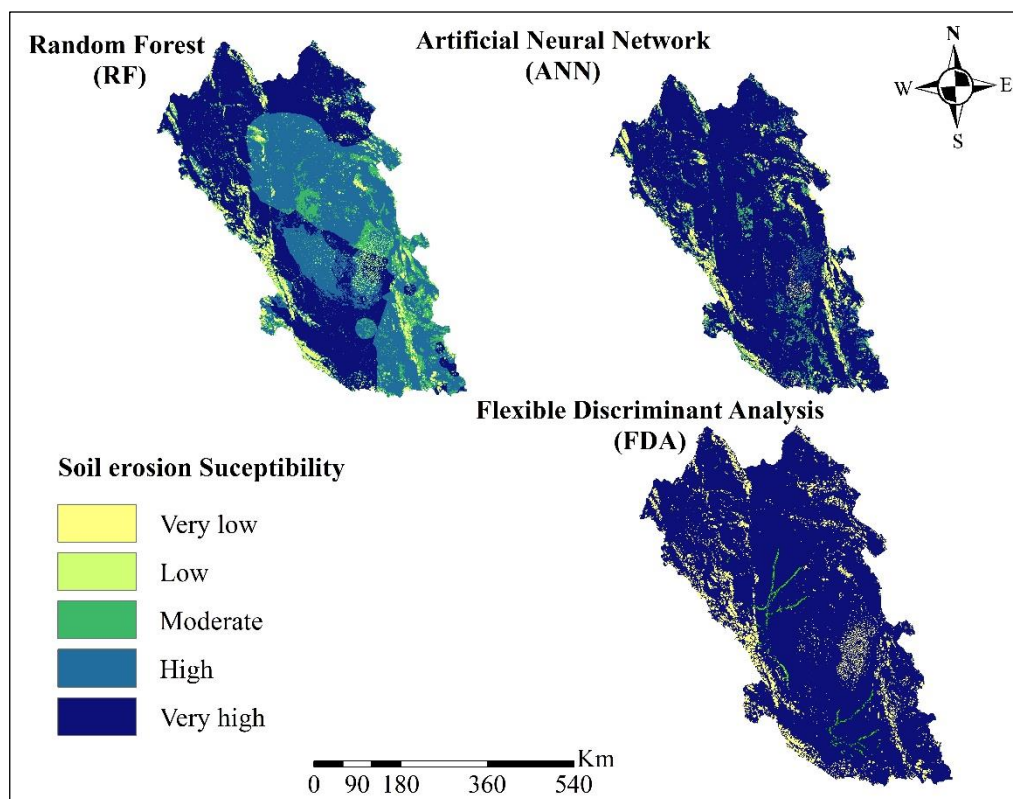
448

### 449 **3.2.2. Spatial modeling of SESA**

450 Fig. 6 shows the SESA predictions from the three machine learning algorithms,  
451 classified by the soil erosion risk in the ArcGIS environment. Validation of the three  
452 machine learning algorithms highlights that RF was again the most reliable algorithm  
453 amongst the three, indicated by the best prediction rate. Based on ROC, RF yields a  
454 94% accuracy for SESA (Fig. 6c). The ROC coefficient of ANN and FDA were slightly  
455 lower, but still high with an accuracy of 91% and 89%, respectively. In the case of the  
456 TSS index, better performance was obtained again for RF (89%) rather than ANN  
457 (78%) and FDA (78%). High performance of RF model in classification issues is related  
458 to its potential to handle big datasets and apply large number of conditioning factors  
459 (Naghibi et al., 2018). In addition, Rahmati et al., 2020 states that high accuracy of RF  
460 is the results of several advantage of this model such as iterative nature and preventing  
461 problems by overfitting (Rahmati et al., 2020).

462 The majority of the land in the watershed (81%) has a high and very high risk for water-  
 463 induced soil erosion by RF. This is slightly lower than for ANN and FDA which  
 464 classified 85% and 89% of the watershed as high and very high susceptible areas. The  
 465 high and very high susceptible areas for water-driven soil erosion are mostly located in  
 466 the north and south-west parts of the watershed. The high and very high susceptible  
 467 areas have socio-economic implications, particularly because most settlements and  
 468 cities of the watershed are located in the same regions. This can mean that human  
 469 activity is a contributing factor to the water-induced soil erosion. Mutually, intensified  
 470 soil erosion might lead to migration of resident people to other places and even other  
 471 countries.

472



473

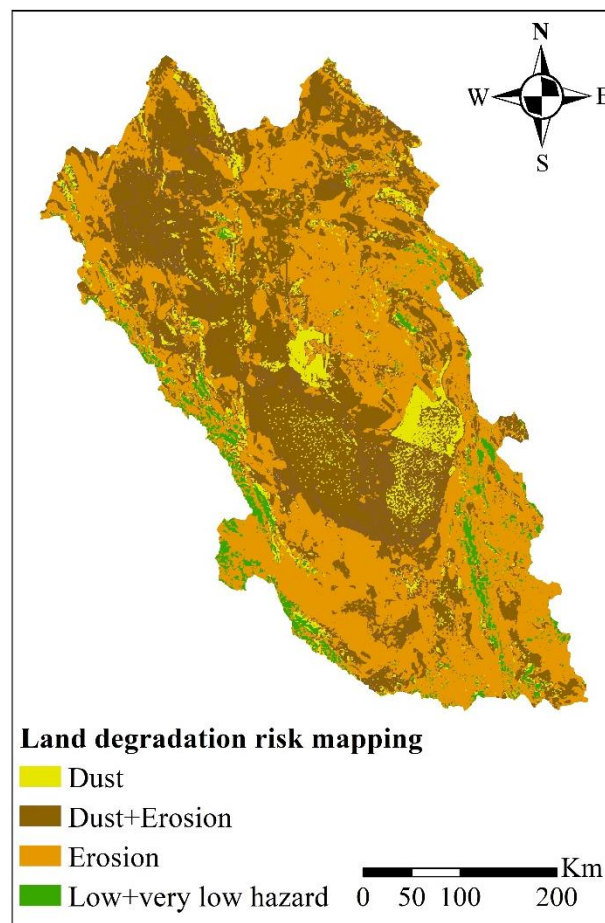
474 Fig. 6 soil erosion susceptibility areas map (GESM) using random forest (RF), artificial neural network  
 475 (ANN), and flexible discriminate analyses (FDA)

476

### 477 3.3. Land degradation susceptibility

478 The majority of the study watershed is susceptible to a substantial risk for land  
 479 degradation. The spatial distribution of land degradation susceptibility, shown in Fig.  
 480 7, indicates that only 4% of the land area has low to very low risks of land degradation.  
 481 Areas susceptible to both soil erosion by water and winds together constitute 43% of

482 the total area. Approximately 45% and 8% of the study area are at risk of soil erosion  
483 by water and wind, respectively. Taken together, it means that the majority of the Lut  
484 watershed falls under the category of land degradation risks. The watershed accounts  
485 for 12.5% of the total land of Iran. The findings of the present study are therefore  
486 consistent with a report that indicated water erosion as an environmental hazard in Iran  
487 (Bui et al. 2019). The results of the study will be helpful and applicable for identifying  
488 water-induced and dust sources hotspots across the watershed and prioritizing  
489 appropriate conservation measurements and rehabilitative policies.  
490 The areas that fall under the category of both kind of land degradation might be most  
491 vulnerable concerning local self-sufficiency for food security and sustainability of  
492 human activities. For instance, dust storms drive water loss through failure of  
493 agricultural crops in Iran (Boroughani et al. 2022). Moreover, the adverse impacts of  
494 water-induced soil erosion are known from numerous other regions (Lal and  
495 Moldenhauer 2008, Gao et al. 2015, Standardi et al. 2018; Roy et al., 2022).



496  
497  
498

Fig. 7 Land degradation susceptibility map in terms of soil erosion and dust sources areas

499 **Conclusion**

500 Investigation of soil erosion through water along with wind-driven soil erosion from  
501 dust sources have received little attention in past studies, despite their importance for  
502 land degradation with associated social, economic, and environmental impacts. The  
503 present study used several different data sets, conducted a field survey and paired the  
504 data with three different machine learning algorithms to construct spatial maps for areas  
505 of risk for land degradation for the Lut watershed in Iran. Three machine learning  
506 algorithms were successfully applied to create land susceptibility maps describing dust  
507 aerosol occurrence considering methodological uncertainty. In addition, these models  
508 were used to identify the areas prone to soil erosion by surface water runoff. These  
509 obtained maps were synthesized to generate a single map for risks of land degradation.  
510 The results of the present study show that the random forest algorithm outperformed  
511 the other two machine learning approaches for both dust sources and soil erosion  
512 susceptibility mapping with an accuracy of 75% and 94%, respectively.  
513 As expected, the vegetation cover, elevation, land use, and geology were important  
514 prerequisites for dust-emission occurrence in the watershed, while rainfall,  
515 Topographical Wetness Index (TWI), terrain slope, terrain elevation, land use, and  
516 geology were identified as the most influential factors for water-induced soil erosion.  
517 Based on the land degradation map, almost the entire study region is at risk. A large  
518 fraction of 43% of the area is prone to both high wind-driven plus water-driven soil  
519 erosion. In addition to these areas, another 45% and 8% of the area have a risk for water-  
520 driven and wind-driven soil erosion, respectively. The methods tested in this study  
521 could be later transferred to similar assessments in other regions around the world.  
522 Choosing this region in Iran is further motivated by the impact of land degradation on  
523 the country's economy. The current study has some limitation including the small  
524 sample size and non-uniform distribution of water-induced soil erosion points because  
525 of lack of accessibility to a road network in some parts of the watershed. Despite these  
526 limitations, these results can potentially be useful for managers and policy makers to  
527 identify local hotspots for land degradation to implement mitigation and adaptation  
528 measures in this watershed. Future studies could work on improving the spatial  
529 resolution and coverage of the risk assessment for providing more information on risks  
530 for land degradation. In addition, it is suggested that future research should estimate the  
531 role of other climatic factors such as humidity, and air temperature on soil erosion and  
532 dust source susceptibility. Prediction of NDVI and rainfall as the most effective factors

533 on soil erosion and dust sources and estimated of their impacts on future water induced-  
534 soil erosion and dust sources susceptibility is also suggested for the other studies. It  
535 requires more measurements for soil erosion by water and winds to train the machine  
536 learning models.

537

### 538 **Acknowledgement**

539 SF acknowledges funding from the German Research Foundation (DFG) for SFB  
540 1502/1–2022 (Project: 450058266).

541

### 542 **Conflict of Interest**

543 The authors declare that there is no conflict of interests regarding the publication of  
544 this article.

545

### 546 **References**

547 Amiri M, Pourghasemi HR, Ghanbarian GA, Afzali SF (2019) Assessment of the importance  
548 of gully erosion effective factors using Boruta algorithm and its spatial modeling and mapping  
549 using three machine learning algorithms. *Geoderma* 340:55–69.  
550 <https://doi.org/10.1016/j.geoderma.2018.12.042>

551 Anache JAA, Flanagan DC, Srivastava A, Wendland EC (2018) Land use and climate change  
552 impacts on runoff and soil erosion at the hillslope scale in the Brazilian Cerrado. *Science of the*  
553 *Total Environment* 622–623:140–151. <https://doi.org/10.1016/j.scitotenv.2017.11.257>

554 Arabameri A, Chen W, Loche M, et al (2019a) Comparison of machine learning models for  
555 gully erosion susceptibility mapping. *Geoscience Frontiers*.  
556 <https://doi.org/10.1016/j.gsf.2019.11.009>

557 Arabameri A, Pradhan B, Rezaei K (2019b) Gully erosion zonation mapping using integrated  
558 geographically weighted regression with certainty factor and random forest models in GIS.  
559 *Journal of Environmental Management* 232:928–942.  
560 <https://doi.org/10.1016/j.jenvman.2018.11.110>

561 Avand M, Moradi HR, Lasbooyee MR (2021) Spatial prediction of future flood risk: An  
562 approach to the effects of climate change. *Geosciences (Switzerland)* 11:1–20.  
563 <https://doi.org/10.3390/geosciences11010025>

564 Beven KJ, Kirkby MJ (1979) A physically based, variable contributing area model of basin  
565 hydrology/Un modèle à base physique de zone d'appel variable de l'hydrologie du bassin  
566 versant. *Hydrological sciences journal* 24:43–69

567 Boroughani M, Mohammadi M, Mirchooli F, Fiedler S (2022) Assessment of the impact of  
568 dust aerosols on crop and water loss in the Great Salt Desert in Iran. *Computers and Electronics*

569 in Agriculture 192:106605

570 Boroughani, M., Pourhashemi, S., Gholami, H., & Kaskaoutis, D. G. 2021. Predicting of dust  
571 storm source by combining remote sensing, statistic-based predictive models and game theory  
572 in the Sistan watershed, southwestern Asia. *Journal of Arid Land*, 13(11), 1103-1121.

573 Boroughani M, Pourhashemi S (2020) Susceptibility Zoning of Dust Source Areas by Data  
574 Mining Methods over Khorasan Razavi Province. *Quarterly journal of Environmental Erosion*  
575 *Research* 9:1–22

576 Boroughani M, Pourhashemi S, Hashemi H, et al (2020) Application of remote sensing  
577 techniques and machine learning algorithms in dust source detection and dust source  
578 susceptibility mapping. *Ecological Informatics* 56:101059.  
579 <https://doi.org/10.1016/j.ecoinf.2020.101059>

580 Breiman L (2001) Random forests. *Machine Learning* 45:5–32.  
581 <https://doi.org/10.1023/A:1010933404324>

582 Bui DT, Shirzadi A, Shahabi H, et al (2019) A novel ensemble artificial intelligence approach  
583 for gully erosion mapping in a semi-arid watershed (Iran). *Sensors (Switzerland)* 19:.  
584 <https://doi.org/10.3390/s19112444>

585 Chicas SD, Omine K, Ford JB (2016) Identifying erosion hotspots and assessing communities  
586 'perspectives on the drivers , underlying causes and impacts of soil erosion in Toledo 's Rio  
587 Grande Watershed : Belize. *Applied Geography* 68:57–67.  
588 <https://doi.org/10.1016/j.apgeog.2015.11.010>

589 Darvand S, Khosravi H, Keshtkar H, et al (2021) Comparison of machine learning models to  
590 prioritize susceptible areas to dust production. *Journal of Range and Watershed Managment*  
591 74:53–68

592 Derakhshan-Babaei F, Mirchooli F, Mohammadi M, et al (2022) Tracking the origin of trace  
593 metals in a watershed by identifying fingerprints of soils, landscape and river sediments.  
594 *Science of The Total Environment* 155583

595 Ebrahimi-khusfi Z, Taghizadeh-mehrjardi R, Mirakbari M (2021) Evaluation of machine  
596 learning models for predicting the temporal variations of dust storm index in arid regions of  
597 Iran. *Atmospheric Pollution Research* 12:134–147. <https://doi.org/10.1016/j.apr.2020.08.029>

598 Emadodin I, Narita D, Rudolf H (2012) Soil degradation and agricultural sustainability : an  
599 overview from Iran. *Environment, Development and Sustainability* 14:611–625.  
600 <https://doi.org/10.1007/s10668-012-9351-y>

601 Gao L, Bowker MA, Xu M, et al (2017) Biological soil crusts decrease erodibility by modifying  
602 inherent soil properties on the Loess Plateau, China. *Soil Biology and Biochemistry* 105:49–  
603 58. <https://doi.org/10.1016/j.soilbio.2016.11.009>

604 Gao X, Xie Y, Liu G, et al (2015) Effects of soil erosion on soybean yield as estimated by  
605 simulating gradually eroded soil profiles. *Soil and Tillage Research* 145:126–134

606 Garosi Y, Sheklabadi M, Conoscenti C, et al (2019) Assessing the performance of GIS- based  
607 machine learning models with different accuracy measures for determining susceptibility to  
608 gully erosion. *Science of the Total Environment* 664:1117–1132.  
609 <https://doi.org/10.1016/j.scitotenv.2019.02.093>

610 Gholami H, Kordestani MD, Li J, et al (2019a) Diverse sources of aeolian sediment revealed  
611 in an arid landscape in southeastern Iran using a modified Bayesian un-mixing model. *Aeolian  
612 Research* 41:100547

613 Gholami H, Mohamadifar A, Sorooshian A, Jansen JD (2020a) Machine-learning algorithms  
614 for predicting land susceptibility to dust emissions : The case of the Jazmurian Basin , Iran.  
615 *Atmospheric Pollution Research* 11:1303–1315. <https://doi.org/10.1016/j.apr.2020.05.009>

616 Gholami H, Mohammadifar A, Collins AL (2019b) Spatial mapping of the provenance of storm  
617 dust: Application of data mining and ensemble modelling Hamid. *Atmospheric Research*  
618 104716. <https://doi.org/10.1016/j.atmosres.2019.104716>

619 Gholami H, Mohammadifar A, Pourghasemi HR, Collins AL (2020b) A new integrated data  
620 mining model to map spatial variation in the susceptibility of land to act as a source of aeolian  
621 dust. *Environmental Science and Pollution Research* 27:42022–42039

622 Ghorbanzadeh O, Kamran KV, Blaschke T, et al (2019) Spatial Prediction of Wildfire  
623 Susceptibility Using Field Survey GPS Data and Machine Learning Approaches. *fire* 2:1–23

624 Gia T, Degener J, Kappas M (2018) Integrated universal soil loss equation ( USLE ) and  
625 Geographical Information System ( GIS ) for soil erosion estimation in A Sap basin : Central  
626 Vietnam. *International Soil and Water Conservation Research* 6:99–110.  
627 <https://doi.org/10.1016/j.iswcr.2018.01.001>

628 Halecki W, Kruk E, Ryczek M (2018) Land Use Policy Loss of topsoil and soil erosion by  
629 water in agricultural areas : A multi- criteria approach for various land use scenarios in the  
630 Western Carpathians using a SWAT model. *Land Use Policy* 73:363–372.  
631 <https://doi.org/10.1016/j.landusepol.2018.01.041>

632 Hosseinalizadeh M, Kariminejad N, Rahmati O, et al (2019) How can statistical and artificial  
633 intelligence approaches predict piping erosion susceptibility? *Science of the Total Environment*  
634 646:1554–1566. <https://doi.org/10.1016/j.scitotenv.2018.07.396>

635 Hahnenberger, M., Nicoll, K., 2014. Geomorphic and land cover identification of dust sources  
636 in the eastern Great Basin of Utah, U.S.A. *Geomorphology* 204 (2), 657–672.  
637 <https://doi.org/10.1016/j.geomorph.2013.09.013>.

638 Jafari M, Mesbahzadeh T, Masoudi R, et al (2021) Dust storm surveying and detection using  
639 remote sensing data, wind tracing, and atmospheric thermodynamic conditions (case study:  
640 Isfahan Province, Iran). *Air Quality, Atmosphere & Health* 1–11

641 Kalantar B, Pradhan B, Naghibi SA, et al (2017) Assessment of the effects of training data  
642 selection on the landslide susceptibility mapping: a comparison between support vector



643 machine (SVM), logistic regression (LR) and artificial neural networks (ANN). *Geomatics,*  
644 *Natural Hazards and Risk* 5705:1–21. <https://doi.org/10.1080/19475705.2017.1407368>

645 Kalantar B, Ueda N, Saeidi V, et al (2020) Landslide susceptibility mapping: Machine and  
646 ensemble learning based on remote sensing big data. *Remote Sensing* 12:1–23.  
647 <https://doi.org/10.3390/rs12111737>

648 Kim JW, Kim HG (2021) Landslide susceptibility analysis by type of cultural heritage site  
649 using ensemble model: Case study of the Chungcheong Region of South Korea. *Sensors and*  
650 *Materials* 33:3819–3833. <https://doi.org/10.18494/SAM.2021.3593>

651 Lal R, Moldenhauer WC (2008) Effects of soil erosion on crop productivity. *Effects of soil*  
652 *erosion on crop productivity* 5:303–367. <https://doi.org/10.1080/07352688709382244>

653 Lee S, Hong S-M, Jung H-S (2017) GIS-based groundwater potential mapping using artificial  
654 neural network and support vector machine models: the case of Boryeong city in Korea.  
655 *Geocarto International* 6049:1–15. <https://doi.org/10.1080/10106049.2017.1303091>

656 Lee, J. A., Gill, T. E., Mulligan, K. R., Acosta, M. D., Perez, A. E. 2009. Land use/land cover  
657 and point sources of the 15 December 2003 dust storm in southwestern North  
658 America. *Geomorphology*, 105(1-2), 18-27

659 Mirchooli F, Motevalli A, Pourghasemi HR, et al (2019) How do data-mining models consider  
660 arsenic contamination in sediments and variables importance? *Environmental Monitoring and*  
661 *Assessment* 191:. <https://doi.org/10.1007/s10661-019-7979-x>

662 Mosavi A, Golshan M, Janizadeh S, et al (2020) Ensemble models of GLM, FDA, MARS, and  
663 RF for flood and erosion susceptibility mapping: a priority assessment of sub-basins. *Geocarto*  
664 *International*. <https://doi.org/10.1080/10106049.2020.1829101>

665 Naghibi SA, Ahmadi K, Daneshi A (2017) Application of Support Vector Machine, Random  
666 Forest, and Genetic Algorithm Optimized Random Forest Models in Groundwater Potential  
667 Mapping. *Water Resources Management* 31:2761–2775. [https://doi.org/10.1007/s11269-017-](https://doi.org/10.1007/s11269-017-1660-3)  
668 1660-3

669 Park S, Kim J, Lee J, et al (2014) Combined dust detection algorithm by using MODIS infrared  
670 channels over East Asia. *Remote Sensing of Environment* 141:24–39.  
671 <https://doi.org/10.1016/j.rse.2013.09.019>

672 Péré J-C, Rivellini L, Crumeyrolle S, et al (2018) Simulation of African dust properties and  
673 radiative effects during the 2015 SHADOW campaign in Senegal. *Atmospheric Research*  
674 199:14–28

675 Rahmati O, Mohammadi F, Saeid S, et al (2020) Identifying sources of dust aerosol using a  
676 new framework based on remote sensing and modelling. *Science of the Total Environment*  
677 737:139508. <https://doi.org/10.1016/j.scitotenv.2020.139508>

678 Rahmati O, Pourghasemi HR, Melesse AM (2016) Application of GIS-based data driven  
679 random forest and maximum entropy models for groundwater potential mapping: A case study

680 at Mehran Region, Iran. *Catena* 137:360–372. <https://doi.org/10.1016/j.catena.2015.10.010>

681 Roy J, Saha S (2019) GIS-based Gully Erosion Susceptibility Evaluation Using Frequency  
682 Ratio , Cosine Amplitude and Logistic Regression Ensembled with fuzzy logic in Hinglo River  
683 Basin , India. *Remote Sensing Applications: Society and Environment* 15:100247.  
684 <https://doi.org/10.1016/j.rsase.2019.100247>

685 Sakizadeh M, Mirzaei R, Ghorbani H (2017) Support vector machine and artificial neural  
686 network to model soil pollution : a case study in Semnan Province , Iran. *Neural Computing  
687 and Applications* 28:3229–3238. <https://doi.org/10.1007/s00521-016-2231-x>

688 Shi P, Yan P, Yuan Y, Nearing MA (2004) Wind erosion research in China: Past, present and  
689 future. *Progress in Physical Geography* 28:366–386.  
690 <https://doi.org/10.1191/0309133304pp416ra>

691 Shit PK, Pourghasemi H reza, Bhunia GS (2020) Gully Erosion Studies from India and  
692 Surrounding Regions

693 Standardi G, Panagos P, Montanarella L, et al (2018) Cost of agricultural productivity loss due  
694 to soil erosion in the European Union : From direct cost evaluation approaches to the use of  
695 macroeconomic models. *Land Degradation & Development* 29:471–484.  
696 <https://doi.org/10.1002/ldr.2879>

697 Sun W, Shao Q, Liu J, Zhai J (2014) Assessing the effects of land use and topography on soil  
698 erosion on the Loess Plateau in China. *Catena* 121:151–163.  
699 <https://doi.org/10.1016/j.catena.2014.05.009>

700 Tehrany MS, Pradhan B, Jebur MN (2014) Flood susceptibility mapping using a novel  
701 ensemble weights-of-evidence and support vector machine models in GIS. *Journal of  
702 Hydrology* 512:332–343. <https://doi.org/10.1016/j.jhydrol.2014.03.008>

703 Yang M, Zhu X, Pan H, et al (2019) Changes of the relationship between spring sand dust  
704 frequency and large-scale atmospheric circulation. *Atmospheric Research* 226:102–109.  
705 <https://doi.org/10.1016/j.atmosres.2019.04.004>

706 Youssef AM, Pourghasemi HR (2021) Landslide susceptibility mapping using machine  
707 learning algorithms and comparison of their performance at Abha Basin, Asir Region, Saudi  
708 Arabia. *Geoscience Frontiers* 12:639–655

709 Zabihi M, Mirchooli F, Motevalli A, et al (2018) Spatial modelling of gully erosion in  
710 Mazandaran Province, northern Iran. *Catena* 161:1–13.  
711 <https://doi.org/10.1016/j.catena.2017.10.010>

712 Zerihun M, Mohammedyasin MS, Sewnet D, et al (2018) Assessment of soil erosion using  
713 RUSLE, GIS and remote sensing in NW Ethiopia. *Geoderma Regional* 12:83–90.  
714 <https://doi.org/10.1016/j.geodrs.2018.01.002>

715 Vickery, K., Eckardt, F. 2013. Dust emission controls on the lower Kuiseb River valley, central  
716 Namib. *Aeolian Res.* 10, 125–133. <https://doi.org/10.1016/j.aeolia.2013.02.006>.

717 Walker, A.L., Liu, M., Miller, S.D., Richardson, K.A., Westphal, D.L., 2009. Development of  
718 a dust source database for mesoscale forecasting in Southwest Asia. *J. Geophys. Res.* 114 (18),  
719 1–24. <https://doi.org/10.1029/2008JD011541>.